Labyrinthine acoustic metamaterials with space-coiling channels for low-frequency sound control

A.O. Krushynska[1,*]**, F. Bosia**[1]**, N.M. Pugno**[2,†]

[1]Department of Physics and Nanostructured Interfaces and Surfaces, University of Torino, Via Pietro Giuria 1, 10125 Torino, Italy

[2]Laboratory of Bio-Inspired and Graphene Nanomechanics, Department of Civil, Environmental and Mechanical Engineering, University of Trento, Via Mesiano 77, 38123 Trento, Italy

17 December 2017

*akrushynska@gmail.com

†nicola.pugno@unitn.it Also at:

(i) School of Engineering and Materials Science, Queen Mary University of London, Mile End Road, London E1 4NS, United Kingdom;

(ii) Ket Labs, Edoardo Amaldi Foundation, Italian Space Agency, Via del Politecnico snc, 00133 Rome, Italy

20

Abstract

We numerically analyze the performance of labyrinthine acoustic metamaterials with internal

channels folded along a Wunderlich space-filling curve to control low-frequency sound in air. In

contrast to previous studies, we perform direct modeling of wave propagation through folded

channels, not introducing effective theory assumptions. As a result, we reveal that metastructures

with channels, which allow wave propagation in the opposite direction to incident waves, have

different dynamics as compared to those for straight slits of equivalent length. The differences

are attributed to activated tortuosity effects and result in 100% wave reflection at band gap

frequencies. This total reflection phenomenon is found to be insensitive to thermo-viscous

dissipation in air. For labyrinthine channels generated by iteration levels, one can achieve

broadband total sound reflection by using a metamaterial monolayer and efficiently control the

amount of absorbed wave energy by tuning the channel width. Thus, the work contributes to a

better understanding of labyrinthine metamaterials with potential applications for reflection and

filtering of low-frequency airborne sound.

1. Introduction

Acoustic metamaterials are composites with an engineered structure governing remarkable functionalities, e.g. acoustic cloaking, transformation acoustics, and subwavelength-resolution imagining [1, 2]. Apart from unusual effective properties, the metamaterials offer various possibilities to control propagation of sound or elastic waves at deep sub-wavelength scales [3, 4, 5]. This can be achieved by incorporating heavy resonators [3], Helmholtz resonators [6, 7], tensioned membranes [8, 9], or sub-wavelength perforations or slits [10, 11, 12, 13] in a material structure. A class of acoustic metamaterials with internal slits is also known as "labyrinthine". They have recently attracted considerable attention due to their abilities to exhibit an exceptionally high refractive index and efficiently reflect sound waves, while preserving light weight and compact dimensions [13, 12, 14].

Labyrinthine metamaterials enable to slow down the effective speed of acoustic waves due to path elongation by means of folded narrow channels [15, 13]. Their high efficiency in manipulating low-frequency sound has been experimentally demonstrated for various channel geometries. For example, Xie et al. [16] have shown the appearance of a negative effective refractive index at broadband frequencies for labyrinthine metastructures with zig-zag-type channels. For the same configuration, Liang et al [15] have demonstrated extraordinary dispersion, including negative refraction and conical dispersion for low-frequency airborne sound. Frenzel et al. have used the zig-zag channels to achieve broadband sound attenuation by means of three-dimensional labyrinthine metastructures [17, 18]. The issue of poor impedance matching for labyrinthine metamaterials has been addressed by exploiting tapered and spiral channels [19] and

89 hierarchically structured walls [20]. 90 Cheng et al. have proven almost perfect 91 reflection of low-frequency sound by 92 sparsely arranged unit cells with circular-93 shaped channels that can induce artificial 94 subwavelength Mie resonances [12]. In 95 our previous work, we have proposed a 96 simple modification to the latter design 97 (by adding a square frame) to achieve a 98 wider tunability [14]. Moleron et al. have 99 emphasized the importance of thermo-100 viscous effects on the performance of 101 labyrinthine structures with sub-102 wavelength slits [21].

103 Most of the studies analyze labyrinthine 104 metamaterials with curved channels by 105 replacing a real system with a simplified 106 one, when dynamics of folded channels is 107 described by that of straight slits of an 108 effective length, which equals to the 109 shortest path taken by a wave within the 110 structure [13, 21, 17, 15, 20]. This 111 approach provides reliable results for 112 channels, in which the direction of wave 113 propagation does not deviate much from

114 that that for incident waves. Therefore, it 115 appears that the channel tortuosity plays 116 no role. Possible effects of the path 117 tortuosity, when a wave is allowed to 118 propagate in the opposite direction 119 relative to that of the incident field, 120 remain to be investigated. A limited 121 number of papers have analyzed 122 labyrinthine metamaterials of this type. 123 In [19], Xie et.al have investigated 124 metastructures with spiral channels to 125 introduce tunability of effective 126 structural parameters, such as refractive 127 index and impedance. Song et. al. have 128 considered hierarchically organized walls 129 to achieve a broadband wave absorption 130 [20]. These works are mainly focused on 131 the experimental validation of the 132 mentioned features, and lack a theoretical 133 analysis of wave behavior in a tortuous 134 channel.

135 The goal of this work is to numerically 136 investigate dispersion and propagation 137 properties of airborne sound in 138 labyrinthine metamaterials with channels

4

139 that allow a change in the direction of
140 wave propagation, and compare their
141 performance with that of the
142 corresponding straight slits. For this
143 purpose, we design sub-wavelength paths
144 in metamaterial unit cells along a
145 hierarchically-organized curve. In
146 particular, we consider a space-filling
147 curve due to its self-similar organization,
148 a simple algorithm to derive length
149 elongation, and an inherent property to
150 fill in occupied area. We provide a
151 complete theoretical analysis of the wave
152 dispersion in the designed metamaterials
153 complemented by the study of acoustic
154 transmission, reflection, and absorption
155 for a mono-slab in the absence or
156 presence of thermo-viscous losses. Our
157 results demonstrate that, when a wave
158 inside a narrow channel is allowed to
159 propagate in the opposite direction with
160 respect to the incident wave front, the
161 wave dynamics is *not equivalen*t to that
162 in a straight slit of an effective length.
163 The peculiar channel tortuosity allows to

164 open sub-wavelength band gaps. At band
165 gap frequencies, total broadband wave
166 reflection occurs that is not influenced by
167 the presence of losses in air. Therefore,
168 the proposed metamaterials have a great
169 potential as efficient reflectors for low-
170 frequency airborne sound. Moreover, to
171 facilitate their practical exploitation, we
172 propose to assemble reconfigurable
173 structures from thin panels of constant
174 thickness (sheets), which is a cheap
175 alternative to an additive manufacturing
176 approach.

177 ## 2. Space-filling curves

178 As mentioned above, the wave path is
179 elongated by exploiting the hierarchical
180 structure of space-filling curves [22].
181 First space-filling curves were
182 discovered by Peano [23] (later named
183 after him), and since then many other
184 curves were proposed [24]. An attractive
185 property of these curves is that they go
186 through every point of a bounding
187 domain for an unlimited number of
188 iterations. After initially being studied as

189 a curiosity, nowadays space-filling
190 curves are widely applied, e.g. for
191 indexing of multi-dimensional data [25],
192 transactions and disk scheduling in
193 advanced databases [26], building
194 routing systems [27], etc.

195 Among various space-filling curves, we
196 have chosen the Wunderlich two-
197 dimensional curve filling a square [22],
198 which is constructed as follows. At the 1st
199 iteration level, one draws an "S"-shaped
200 curve starting at the bottom-left corner of
201 a bounding square and ending at the top-
202 right corner. At the nth ($n \geq 2$) iteration
203 level, 3 copies of the $(n-1)^{th}$-level curve
204 are arranged along each side of a square
205 with every copy being rotated by 90°
206 relative to the previous one. The curves
207 are joined into an N-shaped route starting
208 from the up-direction for the left column,
209 then down for the middle column, and
210 finally again up for the right column. At
211 every iteration level N, the length of the
212 Wunderlich curve is $(3^N - 1/3^N)$, while
213 that of e.g. Hilbert's curves is $(2^N -$

214 $1/2^N)$ [22]. Faster length elongation
215 enables more compact channel folding in
216 a labyrinthine structure (and thus,
217 increases the tortuosity effect, as will be
218 shown later) that justifies the choice of
219 the Wunderlich curve for this study.

3. Models and analysis
methods

222 Figure 1 presents square labyrinths with
223 an internal channel shaped along the
224 Wunderlich curve of the three iteration
225 levels, which are used for constructing
226 "unit cell 1" (UC1), "unit cell 2" (UC2),
227 and "unit cell 3" (UC3), respectively. The
228 structural material is aluminum with
229 mass density $\rho_{Al} = 2700$ kg/m³ and
230 speed of sound $c_{Al} = 5042$ m/s. The
231 thickness of bounding walls is fixed for
232 all the unit cells and equals d=0.5mm.

233 The channel width is w, and the size of a
234 square domain occupied by a single
235 labyrinth is $a = 3^N \cdot (w + d) + d$,
236 where N is the iteration level. We
237 preserve an interconnecting cavity of

238 width w between adjacent labyrinths.

239 Thus, the metamaterial unit cell size is

240 $a_{uc} = a + w$ (see Fig. 1a for notations).

241 We analyze plane waves propagating in

242 the plane of a unit cell cross-section. The

243 metamaterial geometry is assumed to be

244 constant in the out-of-plane direction

245 without a possibility to excite a

246 momentum in this direction. Hence, the

247 pressure field is always constant in the

248 out-of-plane direction, and the wave

249 dynamics can be analyzed by considering

250 a two-dimensional (2D) geometry. The

251 validity of this assumption is confirmed

252 by a good agreement with the results of

253 three-dimensional (3D) simulations

254 given further in the Section 4.

255 First, we analyze sound wave dispersion

256 in the labyrinthine metamaterials that are

257 infinite in both in-plane directions. By

258 neglecting any losses in air, small-

259 amplitude variations of harmonic

260 pressure $p(x, t) = p(x)e^{i\omega t}$ (with

261 angular frequency $\omega = 2\pi f$, where f the

262 frequency in Hz) are governed by the

263 homogeneous Helmholtz equation:

264 $$\nabla \cdot \left(-\frac{1}{\rho_0} \nabla p \right) - \frac{\omega^2 p}{\rho_0 c_0^2} = 0 \qquad (1)$$

265 with air density $\rho_0 = 1.225$ kg/m^3 and

266 speed of sound $c_0 = 343$ m/s at a

267 temperature of $T = 20°C$. Since

268 characteristic acoustic impedance of

269 aluminum is around 4 orders of

270 magnitude larger than that of air, we

271 assume zero displacements for the

272 structural walls and apply sound-hard

273 boundary conditions at air-structure

274 interfaces. The pressure distribution at

275 opposite unit cell boundaries is

276 constrained by the Floquet-Bloch

277 periodic conditions:

278 $$p(x + a) = p(x)e^{ik \cdot a} \qquad (2)$$

279 with $a = (a_{uc}, a_{uc}, 0)$ and wave vector

280 $k = (k_x, k_y, 0)$. More details about the

281 dispersion analysis can be found in [14].

282 Next, we evaluate homogeneous wave

283 propagation through a metamaterial

284 monolayer. Sketch of the model is

285 presented in Fig. 2. Plane wave radiation
286 occurs at the left domain boundary at
287 distance of $10a_{uc}$ from the slab. At the
288 right boundary, a perfectly matched layer
289 of width $2a_{uc}$ is added to eliminate
290 unwanted wave reflection. At the bottom
291 and top boundaries, the Floquet-Bloch
292 periodic boundary conditions (2) enable
293 to artificially extend the air domain in the
294 vertical direction. The reflection $R =$
295 $|p_r/p_i|^2$, transmission $T = |p_t/p_i|^2$, and
296 absorption $A = 1 - R - T$ coefficients
297 are evaluated by averaging incident p_i,
298 reflected p_r, and transmitted p_t pressure
299 fields along the lines located at distance
300 a_{uc} from the structure.

301 In order to analyze how the tortuosity of
302 a labyrinthine channel influences sound
303 wave characteristics, we compare the
304 evaluated T and A values for the
305 metastructures with those for straight slits
306 of width w between solid blocks of length
307 $L=L_{eff}$ or $L=a_{uc}$ distributed at distances a
308 along the vertical direction. In the case of
309 $L=a_{uc}$, the blocks are of the same size as

310 labyrinthine structures, but do not contain
311 internal channels. The effective channel
312 length L_{eff} is approximately equal to the
313 shortest wave path from the input to the
314 output through a labyrinthine channel (as
315 shown e.g. by light-blue lines in Fig. 1b).

316 If a channel width is small compared to
317 the wavelength of a propagating wave,
318 thermal and viscous boundary layers near
319 walls cause loss effects (*lossy* air). The
320 thickness of these layers decreases with
321 increasing frequency. The thickness of
322 thermal boundary layer δ_{th} is evaluated
323 as follows:

$$\delta_{th} = \sqrt{\frac{k}{\pi f \rho_0 C_p}}, \qquad (3)$$

325 where $k = 25.8$ mW/(m·K) is the
326 thermal conductivity, and $C_p = 1.005$
327 kJ/(m³·K) is the heat capacity at constant
328 pressure. The thickness of the viscous
329 boundary layer δ_{vis} is

$$\delta_{vis} = \sqrt{\frac{\mu}{\pi f \rho_0}}, \qquad (4)$$

331 with dynamic viscosity $\mu = 1.814\text{e-}5$
332 Pa·s. The graphical representation of Eqs.

8

333 (3)-(4) is given in Fig. 3. At 20°C and 1
334 atm, the viscous and thermal boundary
335 layers are of thickness 0.22mm and
336 0.26mm at 100 Hz, respectively.

337 As the designed labyrinthine channels are
338 relatively easy to model, we directly
339 include thermal conduction and viscous
340 attenuation into the governing equations.
341 Thus, the linearized system consists of a
342 Navier-Stokes equation, a continuity
343 equation, and an energy equation, which
344 are given in [28]. This system is solved
345 for acoustic pressure variations p, the
346 fluid velocity variations $\boldsymbol{u}$, and the
347 acoustic temperature variations T. The
348 variations describe small harmonic
349 oscillations around a steady state. The
350 mentioned equations are implemented in
351 Thermoacoustic interface of Comsol
352 Multiphysics [29].

353 The dispersion and transmission analyses
354 are performed as eigenvalue and
355 frequency-domain finite-element simula-
356 tions. The described acoustic domains are
357 discretized with the maximum element

358 size of $\lambda_{min}/12$, where $\lambda_{min} = c_0/f_{max}$,
359 and f_{max} is the maximum considered
360 frequency. Such a mesh resolves the
361 smallest wavelength of the study with 12
362 elements. To properly capture the wave
363 field variations within the viscous and
364 thermal boundary layers, we
365 implemented a frequency-varying mesh
366 with 3-5 boundary layers along the
367 thickness of the viscous layer.

368 ## 4. Results and discussion

369 We consider the designed labyrinthine
370 metamaterials of two dimensions. In the
371 first case, defined as a "fixed channel"
372 case, we imply a constant channel width,
373 $w = const$, at each iteration step.
374 Thereby we aim at evaluating effects of
375 tortuosity on sound propagation in
376 elongating paths. For w=4 mm, the
377 metamaterial unit cell sizes are a_{uc} =18
378 mm for UC1, 45 mm for UC2, and 126
379 mm for UC3. For another case, called as
380 "fixed unit cell" case, we assume a fixed
381 unit cell size, $a_{uc} = const$, with the

382 channel width becoming smaller at each
383 iteration. In particular, we fix $a_{uc} = 14$
384 mm that corresponds to the channel width
385 $w = 3$ mm for UC1 and 0.9mm for UC2.
386 For UC3, the internal channel is
387 disappears for the specified wall
388 thickness d=0.5 mm. For the chosen
389 value of a_{uc}, the channel width in the
390 "fixed unit cell" case is smaller than that
391 in the "fixed channel" case at the same
392 iteration level. Thus, by comparing wave
393 propagation for these two cases, we can
394 evaluate how different amount of thermo-
395 viscous losses influences the wave
396 dynamics in labyrinthine channels of the
397 same structure.

398 In the both described cases, an internal
399 labyrinthine channel is shaped along the
400 Wunderlich curve. However, its length is
401 scaled differently than that of the fractal
402 curve due to deviations in construction
403 approaches. Specifically, the algorithm
404 of the Wunderlich curve construction
405 assumes that the curve is a compressing
406 mapping from a low-dimensional space

407 into a 2D domain, the area of which is the
408 same at each iteration level [22]. For our
409 unit cells, we assume the constant wall
410 thickness that incurs variations in the
411 channel length relative to that of the
412 Wunderlich curve. Hence, in the "fixed
413 channel" case, when the area of a
414 bounding square increases at each
415 iteration step (in contrast to the
416 construction approach of the Wunderlich
417 curve), the channel length is elongated by
418 a factor of 3^N relative to a. In the "fixed
419 unit cell" case, the channel length
420 increases as $3^N a - 1$.

4.1 "Fixed-channel" case

422 Figure 4 shows evaluated dispersion
423 relations for homogeneous waves in
424 UC1, UC2, and UC3 propagating along
425 ΓX direction in the reciprocal k-space.
426 The horizontal axis indicates normalized
427 wavenumber $k^* = a_{uc}k$, and the vertical
428 axes depict frequencies f in kHz and
429 normalized frequencies $f^* = f a_{uc}/c_0$.
430 Note different frequency ranges for each

431 unit cell. The analyzed frequencies are
432 limited to a sub-wavelength range, i.e. up
433 to $fa_{uc}/c_0 = 0.5$. For UC1, we consider
434 modes forming the lowest band gap
435 separated into two parts and extending up
436 to 9 kHz. For the UC2 and UC3, the
437 frequency range includes the first 4
438 separated band gaps, and thus, it is
439 limited to 4 kHz and 500 Hz,
440 respectively.

441 The dash-dot lines represent phase
442 velocities of sound waves in lossless air
443 for the lowest fundamental mode within
444 a unit cell (green curve) and in
445 homogeneous air, when a unit cell is
446 removed (red curve). As can be expected,
447 the velocity is reduced when a wave
448 propagates through a labyrinthine
449 channel. The reduction factor is 1.63
450 (UC1), 2.91 (UC2), and 5.28 (UC3)
451 compared to homogeneous air.

452 The dispersion relations in Fig. 4 are
453 characterized by several frequency band
454 gaps in the sub-wavelength region.
455 Hence, the designed labyrinthine

456 metamaterials can control sound waves at
457 sub-wavelength scales. As N increases,
458 the band gaps are shifted down to lower
459 frequencies. The shifts are directly
460 related to the path elongation. For
461 example, the 1st band gap starting from
462 $fa/c_0 = 0.21$ for UC1, is shifted to about
463 3 times lower frequency, $fa/c_0 = 0.069$,
464 for UC2, since the channel length in UC2
465 is 3 times longer than that in UC1.

466 The band-gap bounds are formed by flat
467 parts of dispersion bands that correspond
468 to localized modes. The pressure
469 distributions for these modes are given in
470 the 1st and 3rd columns of Table 1 for the
471 1st band gap bounds and Table 2 for the
472 2nd and 3rd band gap bounds. Red and
473 blue colors represent maximum and
474 minimum values of pressure, while green
475 color indicates near-zero pressure. Strong
476 pressure localization is observed within
477 the labyrinthine channels. It is easy to
478 estimate that regardless of the iteration
479 level, these localized modes correspond

480 to Fabry-Perot resonances in a straight

481 slit of width w and length L_{eff} [21, 13]:

482 $$f_l^{FP} = lc_0/2L_{eff}, \qquad (5)$$

483 where l is a positive integer. In the "fixed

484 channel" case, L_{eff} equals $2.305d_{uc}$ for

485 UC1; $L_{eff} = 5.667d_{uc}$ for UC2, and

486 $L_{eff} = 16.642d_{uc}$ for UC3 with $d_{uc} =$

487 $a_{uc}\sqrt{2}$. Note that odd l values correspond

488 to the lower band gap bounds, while even

489 l values allow approximating the upper

490 band gap bounds in Fig. 4.

491 The fact that multiple Fabry-Perot

492 resonances form the band gap bounds

493 explains a similar structure of the

494 dispersion bands at various frequencies in

495 Fig.4, which have close values of phase

496 and group velocities.

497 The pressure distributions given in

498 Tables 1-2 also resemble those of

499 artificial monopole, dipole and multipole

500 resonances from Ref. [12]. For example,

501 the patterns at lower bound of the 1ˢᵗ band

502 gap (the 1ˢᵗ column in Table 1) is similar

503 to a monopole, in which the pressure is

504 concentrated in the central part of a

505 channel, equally radiating along two

506 propagation directions [12, 14]. Thus, the

507 monopole and multipole resonances in

508 the considered folded channels originate

509 from the tortuosity effect of the Fabry-

510 Perot resonances.

511 Since an effective dynamic bulk modulus

512 (not evaluated in this study) is typically

513 negative at limited frequencies above the

514 monopole resonance, one can expect a

515 high wave reflectance at these

516 frequencies [12]. This behavior has been

517 experimentally observed in [12] for

518 circular-shaped folded channels. The

519 wave transmission and absorption

520 coefficients for our metastructures are

521 discussed below in this section.

522 Apart from the Fabry-Perot resonances,

523 wave dispersion in the designed

524 labyrinthine metamaterials is also

525 characterized by the presence of bands

526 within the band gap frequencies. These

527 bands are found within each band gap for

528 every analyzed unit cell (see curves

529 separating band gaps in Fig. 4). The
530 pressure distributions for these modes
531 (the 2nd column in Tables 1-2) resemble
532 those for the dipole and its higher
533 harmonics (compare to 3rd column of
534 Tables 1-2), but it is not localized inside
535 a channel. Hence, these modes do not
536 represent standing localized waves,
537 rather they are propagating waves with
538 very small (and often negative) group
539 velocities. They may be analogous to
540 slow modes inside phononic band gaps
541 for elastic waves [30, 31]. The
542 mechanism of the slow mode excitation
543 in acoustics and their dynamics will be
544 investigated in more detail in future
545 work. Here, we consider these modes to
546 be included in a single band gap (shown
547 as separated into two parts), since we
548 have not detected the presence of these
549 modes in the frequency-domain
550 simulations (for lossless and lossy air),
551 even for a very fine frequency step (see
552 Figs. 5-6).

553 Frequency-domain simulation results are
554 given in Figs. 5-6 in terms of
555 transmission and absorption coefficients
556 for lossless and lossy air. (Reflection
557 coefficient can be directly derived from
558 these data, and thus is not shown here.)
559 We analyze waves propagating through a
560 monolayer composed of the labyrinthine
561 unit cells (Figs. 5a, 6a, 6c) and periodic
562 straight slits of length L_{eff} (Fig. 5b, 6b,
563 6d) or a_{uc} (Fig. 5c). Note that at certain
564 frequencies for lossy air, the transmission
565 and absorption coefficients appear to be
566 mesh-dependent, and hence are not
567 shown here as unreliable.

568 When losses in air are neglected,
569 incoming waves are either transmitted or
570 reflected for all the considered
571 geometries, and thus, the absorption
572 coefficient is zero (not shown in the
573 graphs). Total transmission is achieved at
574 frequencies of the Fabry-Perot
575 resonances given by Eq. (5). As can be
576 seen, this effect is independent of the
577 channel tortuosity and occurs in folded

578 labyrinthine channels of any iteration
579 level at almost the same frequencies as
580 for straight slits. For the slit of length a_{uc},
581 the fundamental Fabry-Perot resonance
582 appears to be at higher frequencies than
583 the analyzed frequency range. Thus,
584 straight slits of length a_{uc} will be not
585 considered further.

586 When thermo-viscous losses are
587 included, the transmission peaks decrease
588 in magnitude and are shifted to lower
589 frequencies compared to the lossless air.
590 The latter occurs due to the reduction of
591 the propagation velocity in dissipative air
592 and is confirmed by experimental
593 measurements in [21].

594 The striking difference in wave
595 propagation through the unfolded
596 (straight) and hierarchically-structured
597 channels occurs between the frequencies
598 of Fabry-Perot resonances. In case of the
599 straight slits, the main part of incoming
600 waves is reflected, while about 15-20%
601 of the wave energy is transmitted through
602 a slit. For the labyrinthine metamaterials,

603 the same behavior is observed in the
604 propagating frequency range, while
605 within the band gaps total wave reflection
606 occurs with zero transmission coefficient.
607 As mentioned above, at the lower band
608 gap bound, the fundamental Fabry-Perot
609 resonance corresponds to the monopole,
610 and thus, total reflectance is justified by a
611 negative value of effective bulk modulus
612 within the band gap. Experimental data
613 for circular-shaped folded channels [12]
614 show about 84% insertion loss that is in
615 good agreement with the transmission
616 results for straight slits at frequencies
617 between the Fabry-Perot resonances (see
618 e.g. in Fig. 6b). In contrast to this, for our
619 labyrinthine structures total zero
620 transmission is achieved even if thermo-
621 viscous losses are taken into account. We
622 attribute this to the presence of a wave
623 path that redirects a propagating wave in
624 the folded channel to the opposite
625 direction relative to incident waves, since
626 all the other structural parameters (as
627 compared to a straight slit) are the same.

628 Therefore, the peculiar tortuosity of the
629 designed channels significantly modifies
630 the wave dynamics at band-gap
631 frequencies, and these effects cannot be
632 captured by a simplified consideration of
633 equivalent straight slits.

634 While the total transmission at Fabry-
635 Perot resonances is eliminated by the loss
636 mechanisms in air [21], the revealed total
637 reflection at band-gap frequencies is not
638 affected by dissipation. As the iteration
639 level increases, the band gaps, i.e. the
640 total reflection frequencies, are shifted to
641 lower frequencies and decrease in size
642 (compare Figs. 5a, 6a, and 6c). However,
643 the amount of transmitted energy at
644 frequencies of propagating modes also
645 decreases, which is not the case for the
646 straight slits (compare e.g. Figs. 6c and
647 6d). Therefore, the incorporation of third
648 and higher iteration levels for a "fixed
649 channel" unit cell is beneficial for low-
650 frequency sound control and allows to
651 achieve broadband sound reflection.

652 To summarize, we can derive two key
653 conclusions. First, wave propagation in
654 the proposed labyrinthine metamaterials
655 with hierarchically-structured channels
656 differs from that through straight slits of
657 the effective length. The physical
658 mechanism causing this difference is the
659 channel tortuosity, which allows a wave
660 to propagate in the opposite direction
661 relative to an incident pressure field.
662 When deriving effective characteristics
663 for metastructures with complex-shaped
664 wave paths, the mentioned tortuosity
665 effect must be taken into account.
666 Second, the designed labyrinthine
667 metamaterials can be used as broadband
668 low-frequency sound reflectors of
669 compact size, since 100% wave
670 reflection is achieved by using a single
671 unit cell.

672 The circular markers in Fig. 5a represent
673 the transmission coefficient for a
674 corresponding 3D domain obtained by
675 extruding the 2D model (Fig.2) in the
676 out-of-plane direction by a height of

677 $4a_{uc}$. Excellent agreement between the

678 3D and 2D results justifies the introduced

679 assumption of the two-dimensional

680 character of the analyzed problem.

681 Finally, we note that the designed

682 metamaterials can be compared with

683 tortuous open-porous materials. The

684 porosity level, evaluated as the ratio of

685 the area of air inside a unit cell to the total

686 area of a unit cell, is about 90% for UC1,

687 88 % for UC2, and 89 % for UC3, which

688 is rather low as compared to porosity of

689 typical foams slightly deviating from

690 100% [32]. The main difference between

691 porous foams and the designed

692 labyrinthine metamaterials is the physical

693 mechanism of wave control. Porous

694 materials attenuate waves due to inherent

695 thermo-viscous losses with the

696 absorption coefficient close to 1 for broad

697 frequency ranges. In contrast to this, the

698 proposed metastructures mainly reflect

699 incident waves with absorption

700 approaching 0.5 at single frequencies of

701 Fabry-Perot resonances (see Figs. 6 a,c).

702 In the next section, we estimate the

703 metamaterial performance for an

704 increased level of thermo-viscous losses.

4.2 "Fixed-unit-cell" case

706 In the "fixed unit cell" case, the unit cell

707 size $a_{uc} = 14$ mm is fixed as for all the

708 iteration levels. Dispersion relations of

709 UC1 and UC2 are shown in Fig. 7 for

710 homogeneous waves propagating along

711 the ΓX direction. The dimensional

712 frequency ranges here are the same as

713 those for the corresponding unit cells in

714 the "fixed channel" case (see Figs. 4 a,b).

715 The structure of the dispersion relation in

716 Fig. 7a is similar to that in Fig. 4a, except

717 that the bands are shifted to higher

718 frequencies. This occurs due to a shorter

719 channel length. At first sight, more

720 differences are found by comparing the

721 dispersion relations for UC2 in Fig. 4b

722 and Fig. 7b. While in Fig. 4b there are

723 four band gaps, the relation in Fig. 7b is

724 characterized by the presence of a single

725 wide band gap. This happens because the

16

unit cell area, $A^{(fix_{uc})} = 14^2$ mm², in the second case is about 3 times smaller than that for the "fixed channel case", $A^{(fix_w)} = 41^2$mm². As a result, the monopole, dipole and multipole resonances, as well as the related band gaps, are shifted to 3 times higher frequencies. However, in terms of non-dimensional frequencies, the band gap frequencies remain unchanged. The similarity of dispersion relations in Figs. 4 and 7 can be expected, since the metamaterial structure is preserved. In contrast to this, one should observe differences in transmission and absorption coefficients between these two cases due to the different amount of thermo-viscous losses in the channels of a various width.

Figure 8 shows the transmission and absorption coefficients for labyrinthine monoslabs of the "fixed unit cell" case and those for straight slits of the effective length $L_{eff} = 34.5$ mm (UC1) and $L_{eff} = 107$ mm (UC2). The key features found in the analysis of the "fixed channel" case are also observed in the present case, namely the wave propagation in the labyrinthine channels is not equivalent to that in straight slits due to the occurrence of 100% reflection within band gaps. The total reflection is again independent of losses in air. However, as the channel of UC2 in the "fixed unit cell" case is more than 4 times narrower relative to that in the "fixed channel" case, the influence of thermo-viscous losses becomes more pronounced. This can be primarily seen in larger absorption values at the Fabry-Perot resonant frequencies.

Therefore, wave attenuation within labyrinthine channels can be obviously increased by decreasing the channel width. The porosity of the metamaterial then also decreases. For UC2, the structural porosity is 64.7% for the "fixed unit cell" case versus 88% for the "fixed channel" case. Therefore, one can consider the wave absorption within the labyrinthine metamaterials as similar to

776 that of tortuous foams by decreasing the

777 structural external dimensions and

778 porosity level.

5. Conclusions

780 In this work, we have theoretically

781 analyzed the possibilities of labyrinthine

782 acoustic metamaterials with sub-

783 wavelength channels shaped along a

784 space-filling curve to control airborne

785 homogeneous sound. We have

786 demonstrated that, if a folded channel

787 allows wave propagation in an opposite

788 direction compared to incident pressure,

789 wave dynamics in the channel is not

790 equivalent to that of a straight slit of an

791 effective length. In particular, we have

792 shown that Fabry-Perot resonances of the

793 straight slit correspond to monopole,

794 dipole and multipole resonances in folded

795 channels and govern the generation of

796 band gaps. Within the band gaps, total

797 wave reflection occurs that is not

798 influenced by the presence of dissipation

799 in air. Moreover, by increasing the

800 channel tortuosity and further elongating

801 a wave path, one can achieve almost

802 perfect reflection outside the band gaps.

803 Although at higher iteration levels the

804 designed metamaterials resemble a

805 tortuous porous material, they mostly

806 control waves due to interference effects,

807 in contrast to thermo-viscous dissipation

808 mechanism in porous foams. This results

809 in a low wave attenuation within a

810 metastructure for a sufficiently wide

811 channel. The absorption level can be

812 increased by decreasing the channel

813 width and the structural weight.

814 This is the first time that a space-filling

815 curve has been considered for designing

816 and elongating wave paths in labyrinthine

817 metamaterials. Therefore, further more

818 in-depth analysis is required to study the

819 influence of various geometric factors,

820 e.g. number or angles of turns, as well as

821 the metamaterial performance for

822 inhomogeneous waves in complex-

823 shaped folded channels. These studies

824 will be performed in future works. The

825 proposed structures show promise as

826 broadband low-frequency sound

827 reflectors that can be inexpensively

828 assembled from thin sheets.

829 Acknowledgements

References

[1] S. Cummer, J. Christensen and A. Alu, "Controlling sound with acoustic metamaterials," *Nat. Rev. Mats.,* vol. 16001, 2016.

[2] R. V. Craster and S. Guenneau, Acoustic Metamaterials: Negative Refraction, Imaging, Lensing and Cloaking, Heidelberg: Springer, 2012.

[3] Z. Liu, X. Zhang, Y. Mao, Y. Y. Zhu, Z. Yang, C. Chan and P. Sheng, "Locally resonant sonic materials," *Science,* vol. 289, p. 1734, 2000.

[4] A. Krushynska, V. Kouznetsova and M. Geers, "Towards optimal design of locally resonant acoustic metamaterials," *J. Mech. Phys. Solids,* vol. 71, p. 179–196, 2014.

[5] P. Deymier, Acoustic metamaterials and phononic structures, Heidelberg: Springer, 2013.

[6] N. Fang, D. Xi, J. Xu, M. Ambati, W. Srituravanich, C. Sun and X. Zhang, "Ultrasonic metamaterials with negative modulus," *Nat. Mat.,* vol. 5, pp. 452-456, 2006.

[7] A. Movchan and S. Guenneau, "Split-ring resonators and localized modes," *Phys. Rev. B,* vol. 70, p. 125116, 2004.

[8] G. Ma, M. Yang, S. Xiao, Z. Yang and P. Sheng, "Acoustic metasurface with hybrid resonances," *Nat. Mat.,* vol. 13, pp. 873-878, 2014.

[9] Z. Yang, J. Mei, M. Yang, N. H. Chan and P. Sheng, "Membrane-type acoustic metamaterial with negative dynamic mass," *Phys. Rev. Lett.,* vol. 101, p. 204301, 2008.

[10] V. García-Chocano and J. Sánchez-Dehesa, "Anomalous sound absorption in lattices of cylindrical perforated shells," *Appl. Phys. Lett.,* vol. 106, no. 12, p. 124104, 2015.

[11] A. Bozhko, J. Sanchez-Dehesa and A. Krokhin, "Redirection and splitting of sound waves by a periodic chain of thin perforated cylindrical shells," *J. Acoust. Soc. Am.,* vol. 141, p. 3640, 2017.

[12] Y. Cheng, C. Zhou, B. Yuan, D. Wu, Q. Wei and X. Liu, "Ultra-sparse metasurface for high reflection of low-frequency sound based on artificial Mie resonances," *Nat. Mater.,* vol. 14, pp. 1013-1019, 2015.

[13] Z. Liang and J. Li, "Extreme acoustic metamaterial by coiling up space," *Phys. Rev. Lett.,* vol. 108, p. 114301, 2012.

[14] A. Krushynska, F. Bosia, M. Miniaci and N. Pugno, "Tunable spider-web inspired hybrid labyrinthine acoustic metamaterials for low-frequency sound control," *arXiv:1701.07622,* 2017.

[15] Z. Liang, T. Feng, S. Lok, F. Liu, K. Ng, C. Chan, J. Wang, S. Han, S. Lee and J. Li, "Space-coiling metamaterials with double negativity and conical dispersion," *Sci. Rep.,* vol. 3, p. 1614, 2013.

[16] Y. Xie, B.-I. Popa, L. Zigoneanu and S. Cummer, "Measurement of a broadband negative index with space-coiling acoustic metamaterials," *Phys. Rev. Lett.,* vol. 110, p. 175501, 2013.

[17] T. Frenzel, J. Brehm, T. Bueckmmmann, R. Schitty, M. Kadic and M. . Wegener, "Three-dimensional labyrinthine acoustic metamaterials," *Appl. Phys. Lett.,* vol. 103, p. 061907, 2013.

[18] C. Zhang and X. Hu, "Three-dimensional single-port labyrinthine acoustic metamaterial: perfect absorption with large bandwidth and tunability," *Phys. Rev. Appl.,* vol. 6, p. 064025, 2016.

[19] Y. Xie, A. Konneker, B.-I. Popa and S. Cummer, "Tapered labyrinthine acoustic metamaterials for broadband impedance matching," *Apl. Phys. Lett.,* vol. 103, p. 201906, 2013.

[20] G. Song, Q. Cheng, B. Huang, H. Y. Dong and T. Cui, "Broadband fractal acoustic metamaterials for low-frequency sound attenuation," *Appl. Phys. Lett.,* vol. 109, p. 131901, 2016.

[21] M. Moleron, M. Serra-Garcia and C. Daraio, "Visco-thermal effects in acoustic metamaterials: from total transmission to total reflection and high absorption," *New J. Phys.,* vol. 18, p. 033003, 2016.

[22] H. Sagan, Space-filling curves, Springer, 1994.

[23] G. Peano, "Sur une courbe, qui remplit toute une aire plane," *Math. Ann.,* vol. 36, no. 1, pp. 157-160, 1890.

[24] H. Haverkort and F. van Walderveen, "Locality and bounding-box quality of two-dimensional," *Computational Geometry: Theory and Applications,* vol. 43, pp. 131-147, 2010.

[25] J. K. Lawder and P. J. H. King, "Using Space-Filling Curves for Multi-dimensional Indexing," *Advances in Databases. BNCOD 2000. Lecture Notes in Computer Science,* vol. 1832, 2000.

[26] M. Ali and S. Ladhake, "Overview of space-filling curves and their applications in scheduling," *International Journal of Advances in Engineering and Technology,* vol. 1, no. 4, pp. 148-154, 2011.

[27] L. Platzman and J. I. Bartholdi, "Spacefilling curves and the planar travelling salesman problem," *Journal of the ACM,* vol. 36, no. 4, pp. 719-737, 1989.

[28] Acoustics Module of Comsol Multiphyscis. User's guide, 2013.

[29] R. 5. Comsol Multiphysics. [Online]. Available: www.comsol.com.

[30] R. Zhu, X. Liu, G. Hu, F. Yuan and G. Huang, "Microstructural designs of plate-type elastic metamaterial and their potential applications: a review," *Int. J. Smart and Nano Mater.,* vol. 6, no. 1, pp. 14-40, 2015.

[31] C.-Y. Sun, J.-C. Hsu and T. Wu, "Resonant slow modes in phononic crystal plates with periodic membranes," *Appl. Phys. Lett.,* vol. 97, p. 031902, 2010.

[32] J. Allard and N. Atalla, Propagation of sound in porous media: modelling sound absorbing materials, Willey, 2009.

List of figures

Figure 1. (a) Unit cell of the 1st iteration level (UC1) with dimensions. (b-d) Labyrinths with air channels shaped according to the Wunderlich space-filling curve of the first three iteration levels incorporated into UC1, UC2, and UC3. Solid walls are indicated in blue. The shortest path taken by a wave within UC1 is shown by blue arrows in (b).

Figure 2. Schematic of the frequency domain model. Green area corresponds to an air domain, green dashed lines indicate locations, at which reflection and transmission coefficients are evaluated. The plane wave radiation condition is applied along the bold red line.

Figure 3. Thickness of viscous δ_{vis} and thermal δ_{th} boundary layers according to relations (3) and (4).

Figure 4. **"Fixed channel" case**: Dispersion relations for the labyrinthine unit cells of the 3 iteration levels with a fixed channel width, w=4 mm. Band gaps are shown by shaded rectangles. The slope of the green and red dash-dot lines indicates phase velocities of the fundamental mode

within a unit cell and in homogenous air (when a unit cell is removed). Bold points designate frequencies with the pressure distributions given in Table 1 and 2.

Figure 5. **"Fixed channel" case:** Transmission (T) and absorption (A) coefficients for acoustic waves in lossless (dashed line) and lossy (solid line) air through (a) a labyrinthine metamaterial UC1; (b) a straight slit of width w = 4 mm and length L_{eff} = 45.6 mm; (b) a straight slit of width w = 4 mm and length a_{uc} = 18 mm. Shaded regions indicate frequency a band gap shown in Fig. 4a. Circular markers in (a) indicate transmission coefficient values in lossless air for the corresponding 3D model of height $4a_{uc}$.

Figure 6. **"Fixed channel" case:** Transmission (T) and absorption (A) coefficients for acoustic waves in lossless (dotted line) and lossy (solid line) air through (a) a labyrinthine metamaterial UC2 and (b) a straight slit of width w = 4 mm and length L_{eff} = 328.5 mm; (c) a labyrinthine unit cell UC3 and (d) a straight slit of width w = 4 mm and length L_{eff} = 2.871 m. Shaded regions indicate frequency band gaps shown in Fig. 4.

Figure 7. **"Fixed unit cell" case**: Band structure diagrams for the unit cells UC1 and UC2 of fixed size a=14 mm with the channel width of 3 mm and 0.9 mm, respectively. Band gap frequencies are shaded. The slopes of the green and red dash-dot lines indicate the phase velocities of the fundamental pressure wave inside a unit cell and in homogeneous air (when a unit cell is removed).

Figure 8. **"Fixed unit cell" case:** Transmission (T) and absorption (A) coefficients for acoustic waves in lossless (dotted line) and lossy (solid line) air through (a) a labyrinthine unit cell UC1 and (b) a straight slit of width $w = 3$ mm and length $L_{eff} = 34.6$ mm; (c) a labyrinthine unit cell UC2 and (d) a straight slit of width $w = 0.9$ mm and length $L_{eff} = 107$ mm. Shaded regions indicate frequency band gaps shown in Fig. 7.

List of tables

Table 1. **"Fixed channel" case ("Fixed unit cell" case):** Pressure distributions around the 1st band gap for the labyrinthine metamaterial unit cells of the 3 iteration levels. Red and blue colors represent maximum and minimum pressure, while green color indicates (almost) zero pressure. The frequencies in brackets are referred to the "fixed unit cell" case.

Table 2. **"Fixed channel" case**: Pressure distributions around the 2nd and 3rd band gaps for the labyrinthine metamaterial unit cells of the 2nd and 3rd iteration levels. Red and blue colors represent maximum and minimum pressure, and green color indicates (almost) zero pressure.

Figures

(a) UC1

(c) 2nd iteration

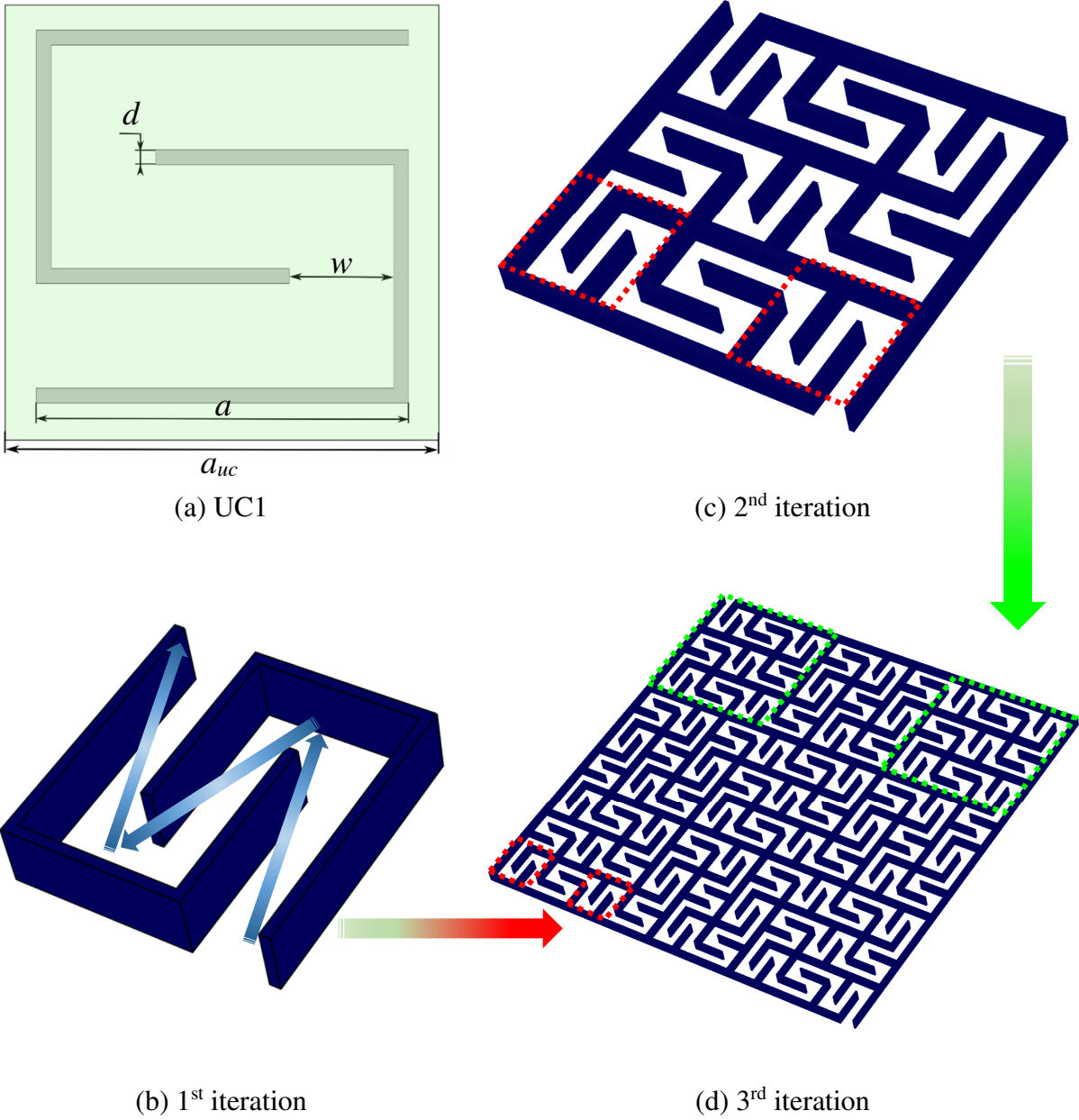(b) 1st iteration

(d) 3rd iteration

Figure 1. (a) Unit cell of the 1st iteration level (UC1) with dimensions. (b-d) Labyrinths with air channels shaped according to the Wunderlich space-filling curve of the first three iteration levels incorporated into UC1, UC2, and UC3. Solid walls are indicated in blue. The shortest path taken by a wave within UC1 is shown by blue arrows in (b).
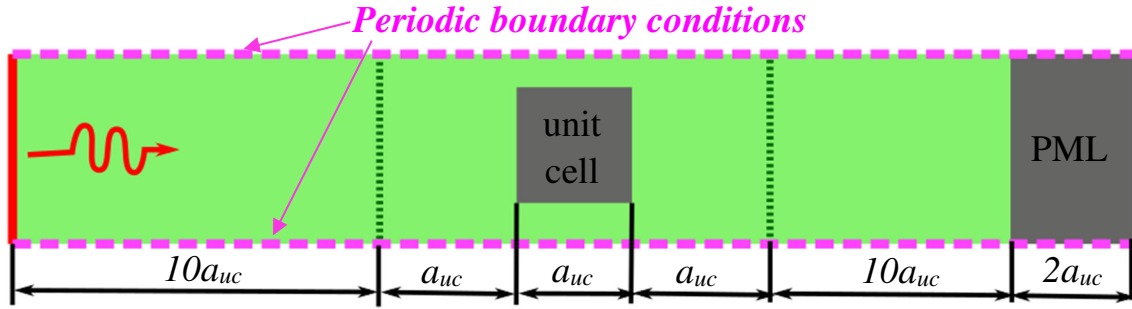
Figure 2. Schematic of the frequency domain model. Green area corresponds to an air domain, green dashed lines indicate locations, at which reflection and transmission coefficients are evaluated. The plane wave radiation condition is applied along the bold red line.
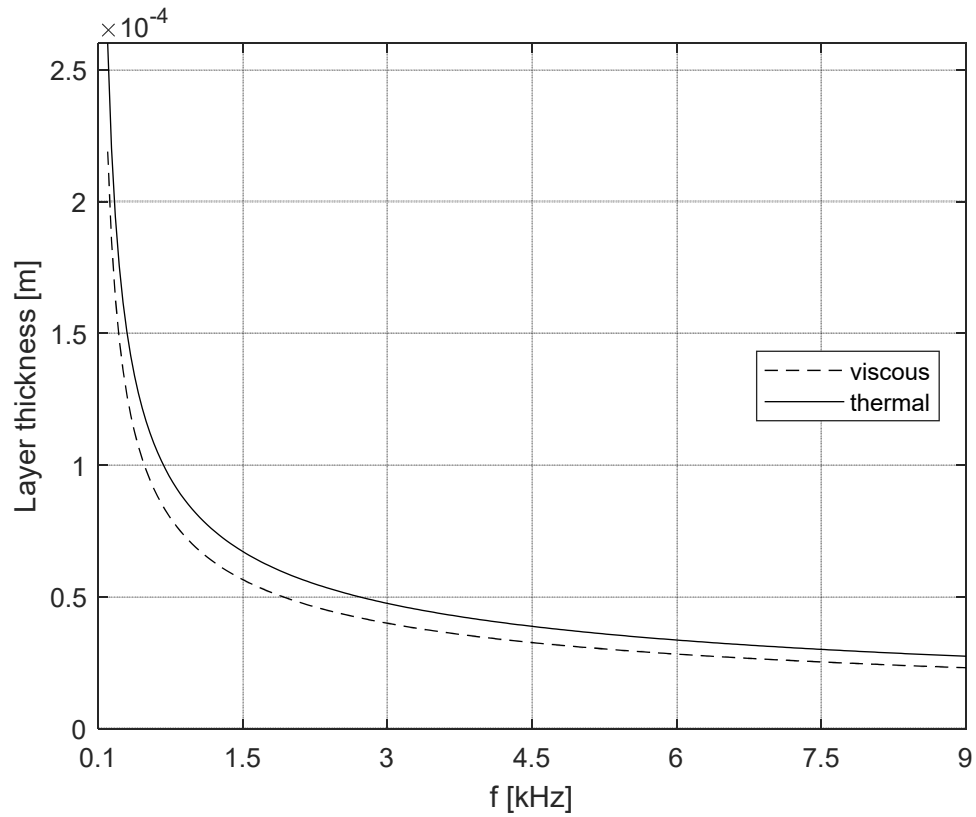

Figure 3. Thickness of viscous δ_{vis} and thermal δ_{th} boundary layers according to relations (3) and (4).
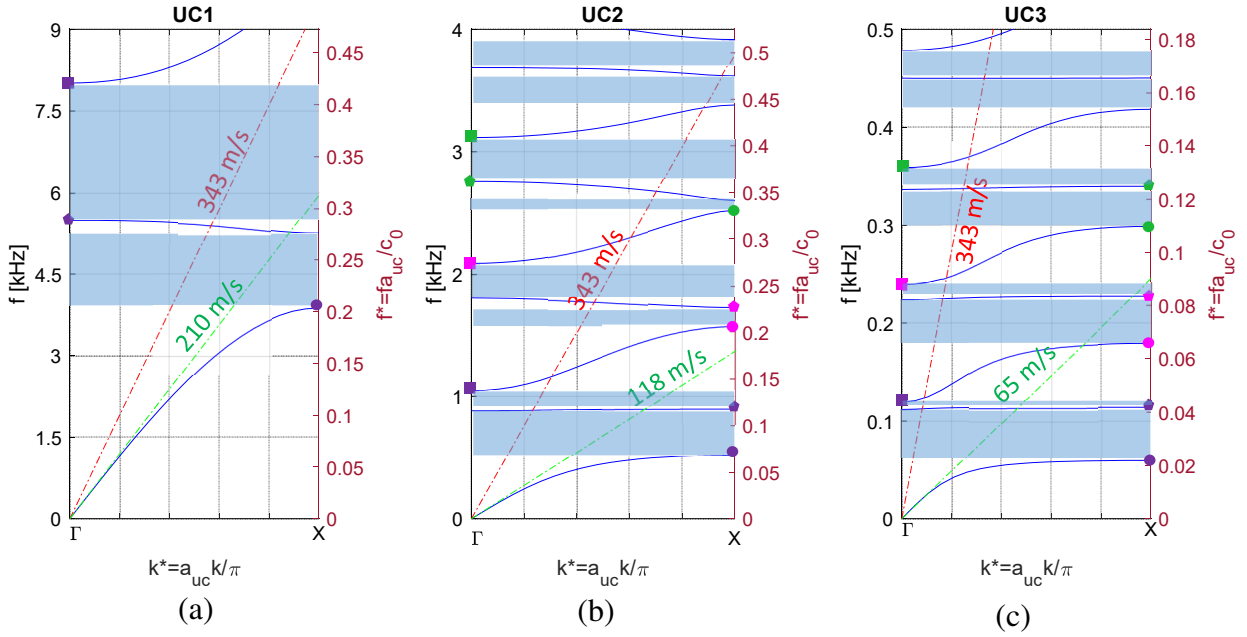
*Figure 4. **"Fixed channel" case**: Dispersion relations for the labyrinthine unit cells of the 3 iteration levels with a fixed channel width, w=4 mm. Band gaps are shown by shaded rectangles. The slope of the green and red dash-dot lines indicates phase velocities of the fundamental mode within a unit cell and in homogenous air (when a unit cell is removed). Bold points designate frequencies with the pressure distributions given in Table 1 and 2.*

*Table 1. **"Fixed channel" case ("Fixed unit cell" case):** Pressure distributions around the 1st band gap for the labyrinthine metamaterial unit cells of the 3 iteration levels. Red and blue colors represent maximum and minimum pressure, while green color indicates (almost) zero pressure. The frequencies in brackets are referred to the "fixed unit cell" case.*
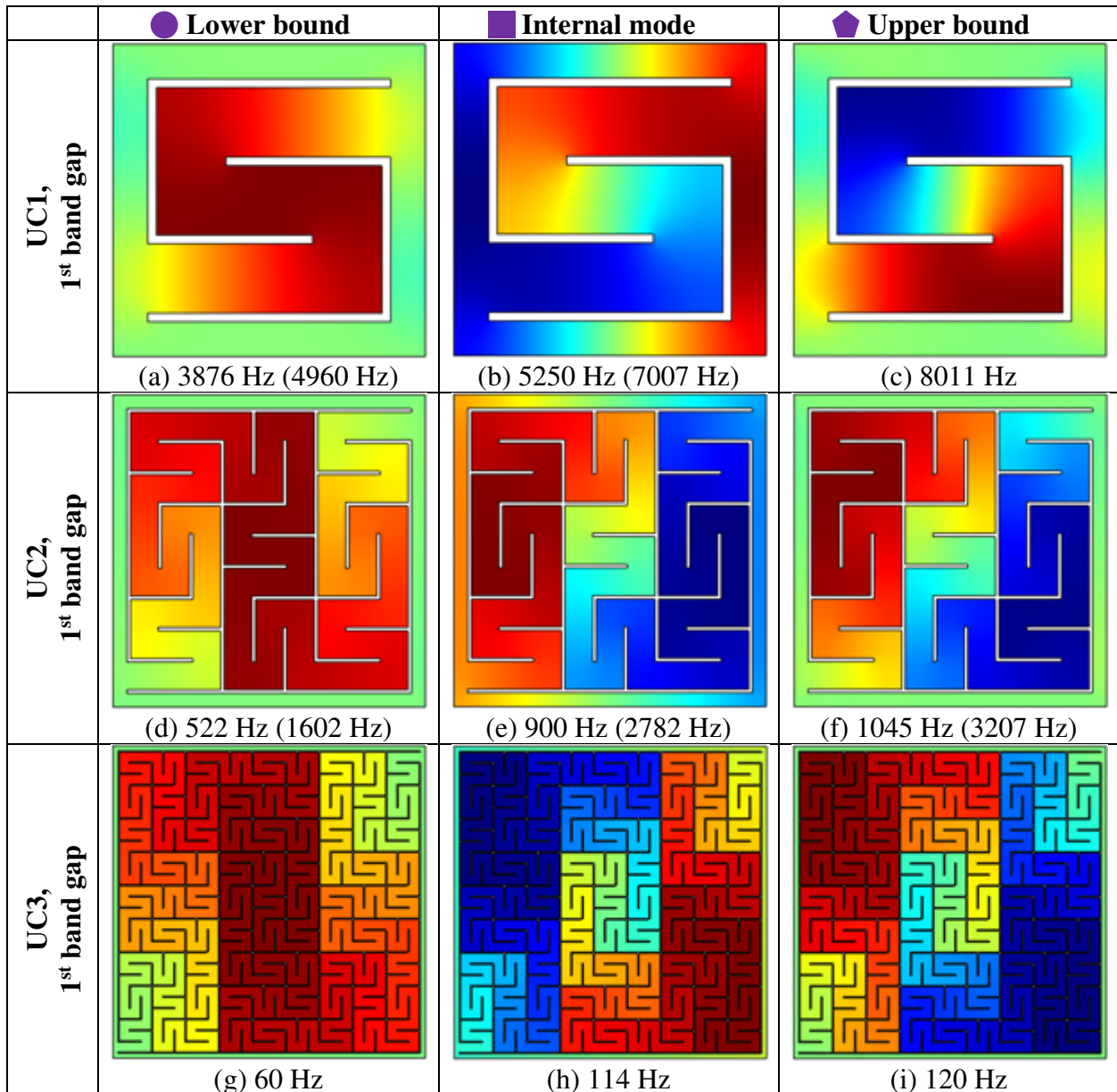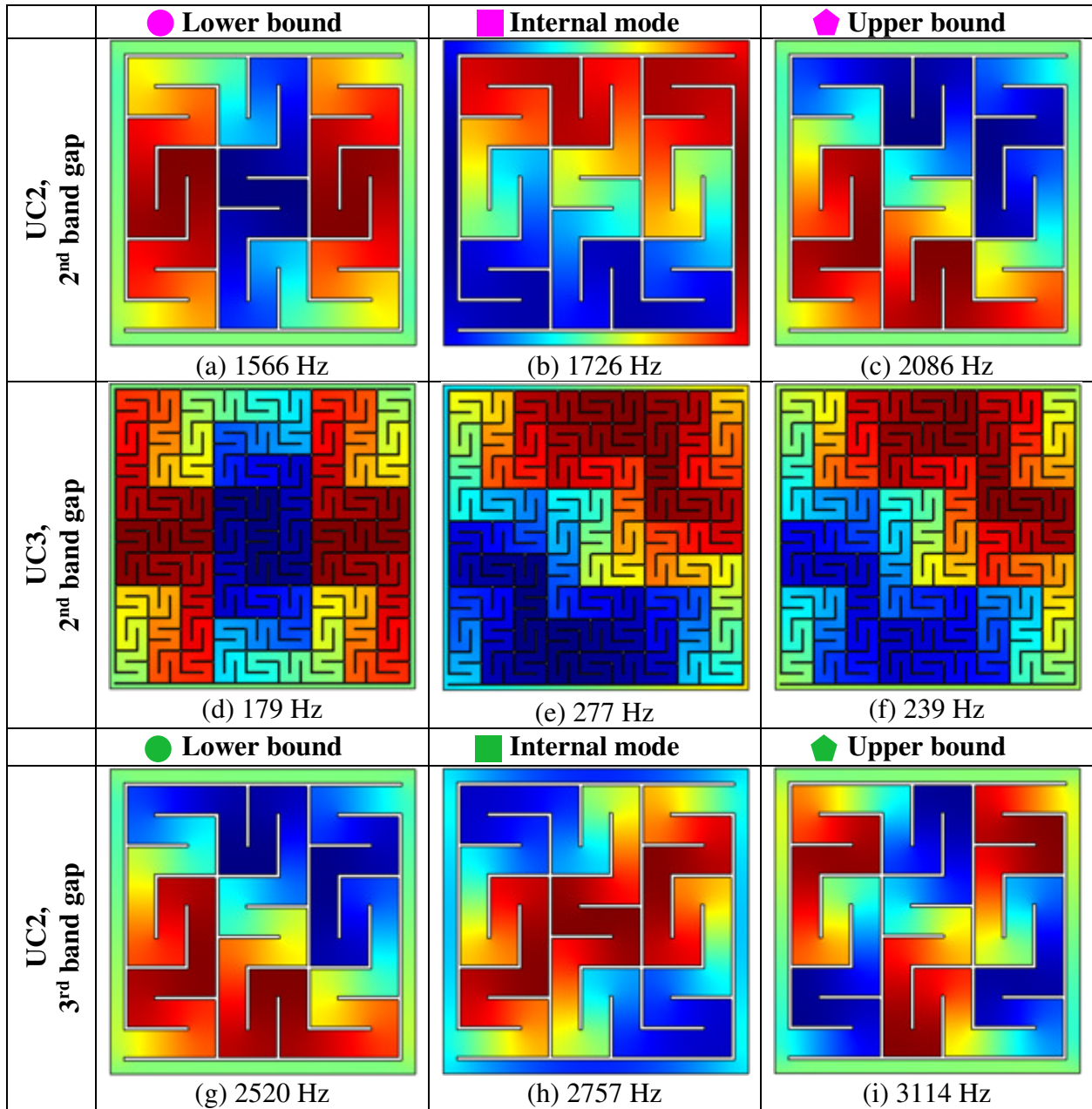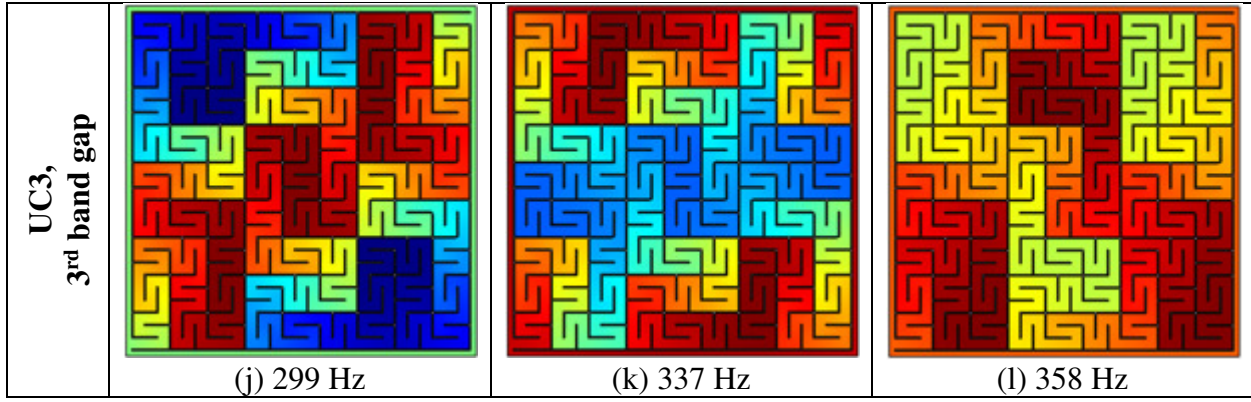
	● **Lower bound**	■ **Internal mode**	⬠ **Upper bound**
UC1, 1st band gap	(a) 3876 Hz (4960 Hz)	(b) 5250 Hz (7007 Hz)	(c) 8011 Hz
UC2, 1st band gap	(d) 522 Hz (1602 Hz)	(e) 900 Hz (2782 Hz)	(f) 1045 Hz (3207 Hz)
UC3, 1st band gap	(g) 60 Hz	(h) 114 Hz	(i) 120 Hz

*Table 2. **"Fixed channel" case**: Pressure distributions around the 2ⁿᵈ and 3ʳᵈ band gaps for the labyrinthine metamaterial unit cells of the 2ⁿᵈ and 3ʳᵈ iteration levels. Red and blue colors represent maximum and minimum pressure, and green color indicates (almost) zero pressure.*
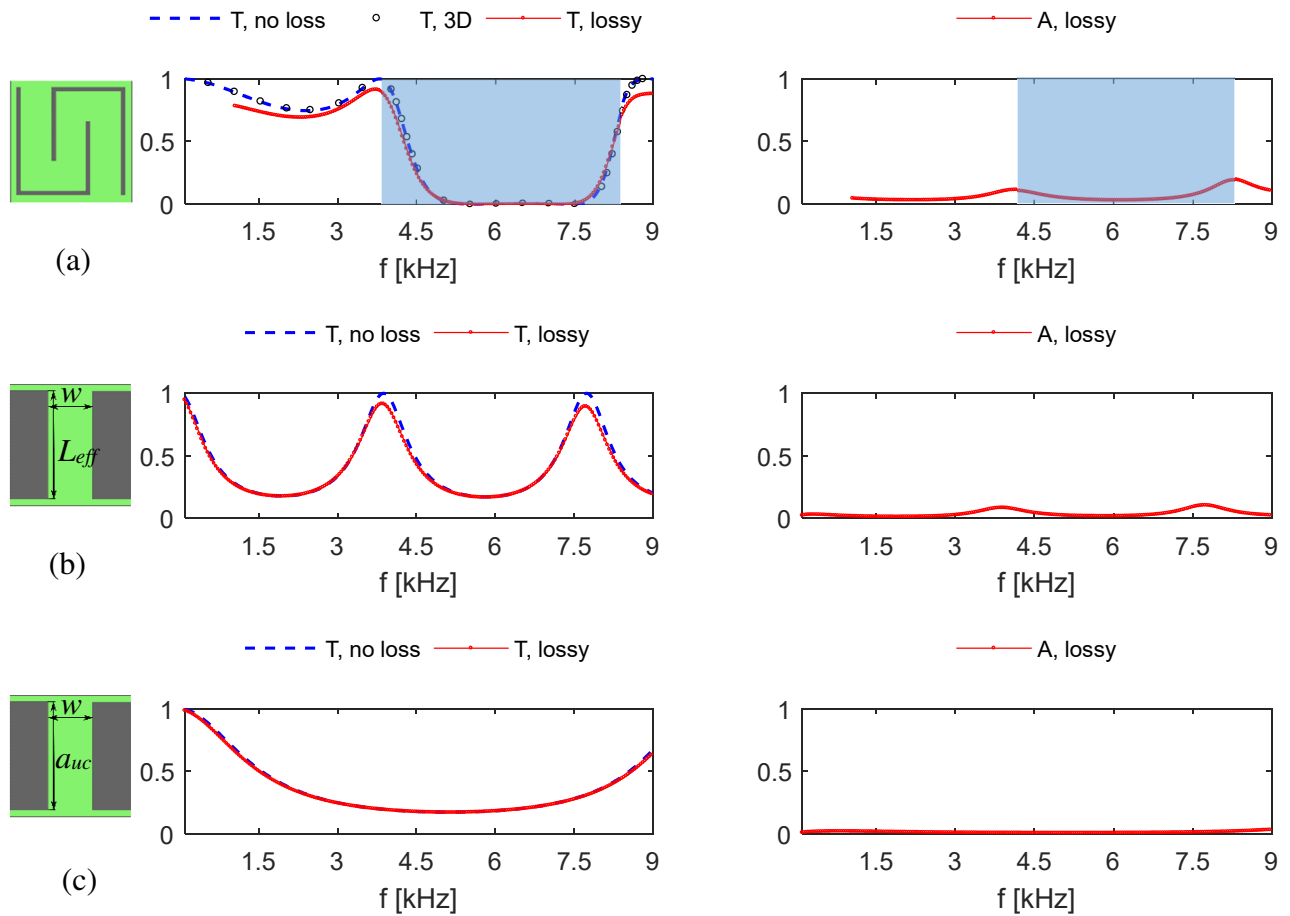
● **Lower bound**	■ **Internal mode**	⬠ **Upper bound**
UC2, 2ⁿᵈ band gap		
(a) 1566 Hz	(b) 1726 Hz	(c) 2086 Hz
UC3, 2ⁿᵈ band gap		
(d) 179 Hz	(e) 277 Hz	(f) 239 Hz
● **Lower bound**	■ **Internal mode**	⬠ **Upper bound**
UC2, 3ʳᵈ band gap		
(g) 2520 Hz	(h) 2757 Hz	(i) 3114 Hz

| | (j) 299 Hz | (k) 337 Hz | (l) 358 Hz |
| UC3, 3rd band gap | | | |

*Figure 5. **"Fixed channel" case:** Transmission (T) and absorption (A) coefficients for acoustic waves in lossless (dashed line) and lossy (solid line) air through (a) a labyrinthine metamaterial UC1; (b) a straight slit of width w = 4 mm and length L_{eff} = 45.6 mm; (b) a straight slit of width w = 4 mm and length a_{uc} = 18 mm. Shaded regions indicate a frequency band gap. Circular markers in (a) indicate transmission coefficient values in lossless air for the corresponding 3D model of height $4a_{uc}$.*
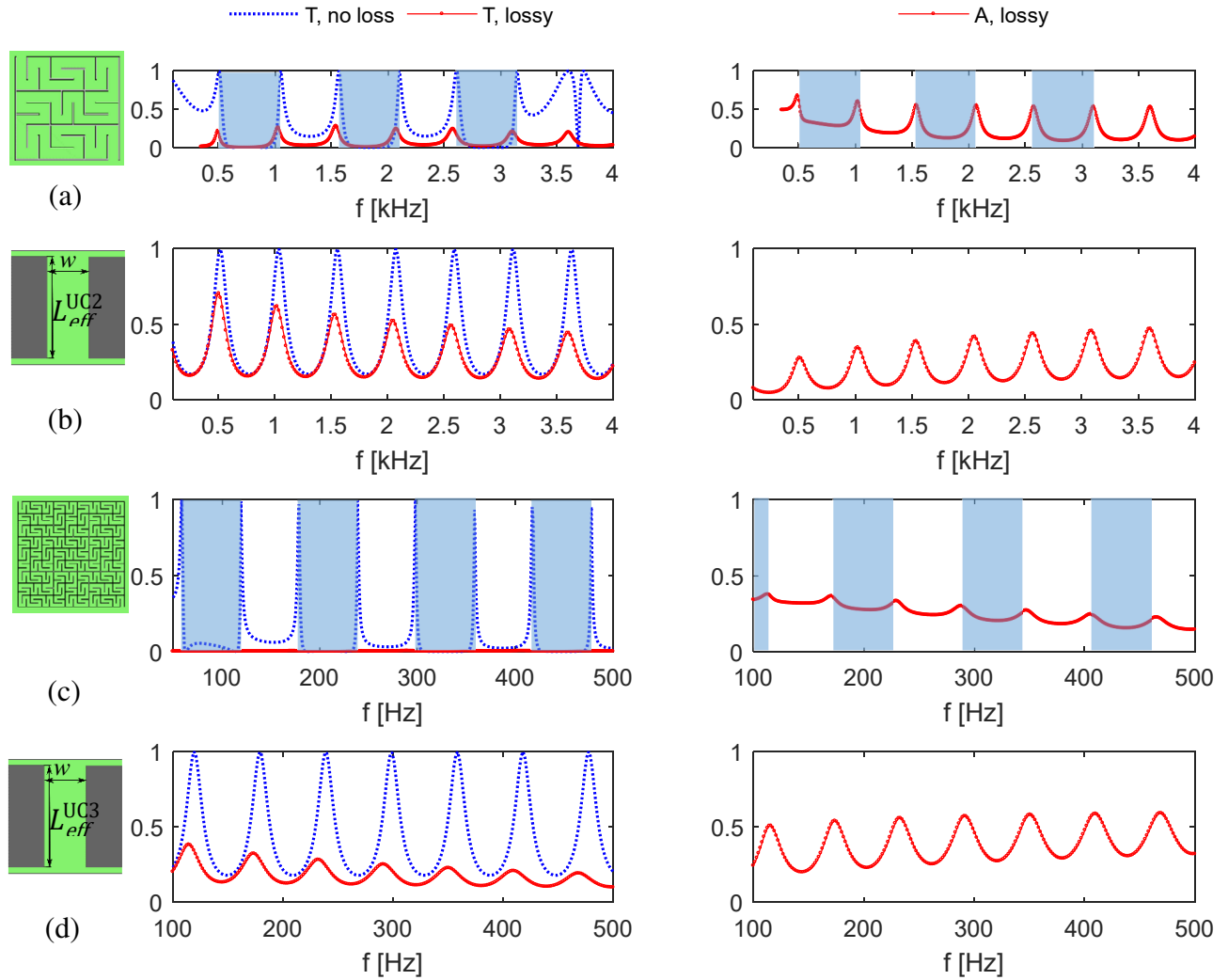
Figure 6. "Fixed channel" case: Transmission (T) and absorption (A) coefficients for acoustic waves in lossless (dotted line) and lossy (solid line) air through (a) a labyrinthine metamaterial UC2 and (b) a straight slit of width w = 4 mm and length L_eff = 328.5 mm; (c) a labyrinthine unit cell UC3 and (d) a straight slit of width w = 4 mm and length L_eff = 2.871 m. Shaded regions indicate frequency band gaps.
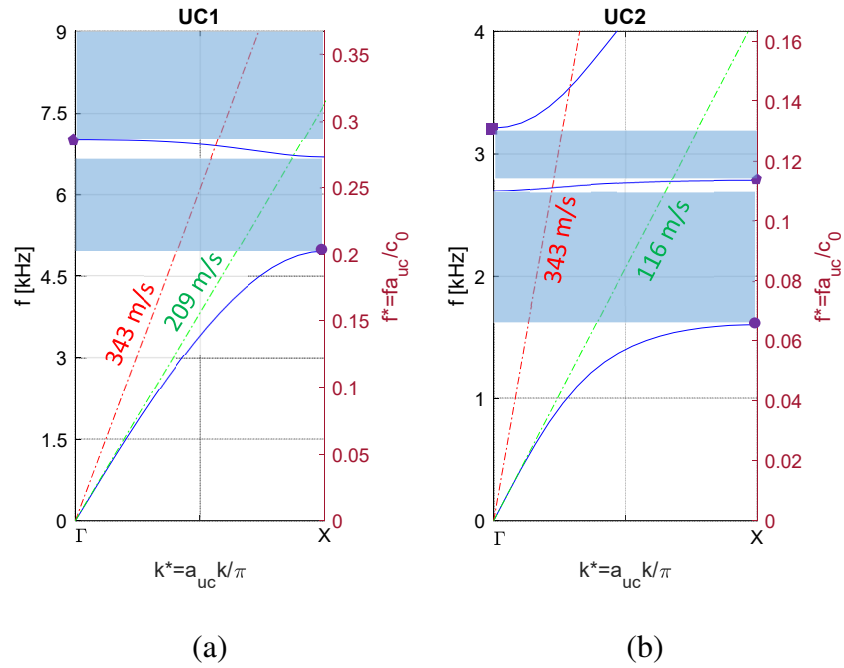
8

*Figure 7. **"Fixed unit cell" case**: Band structure diagrams for the unit cells UC1 and UC2 of fixed size a=14 mm with the channel width of 3 mm and 0.9 mm, respectively. Band gap frequencies are shaded. The slopes of the green and red dash-dot lines indicate the phase velocities of the fundamental pressure wave inside a unit cell and in homogeneous air (when a unit cell is removed).*
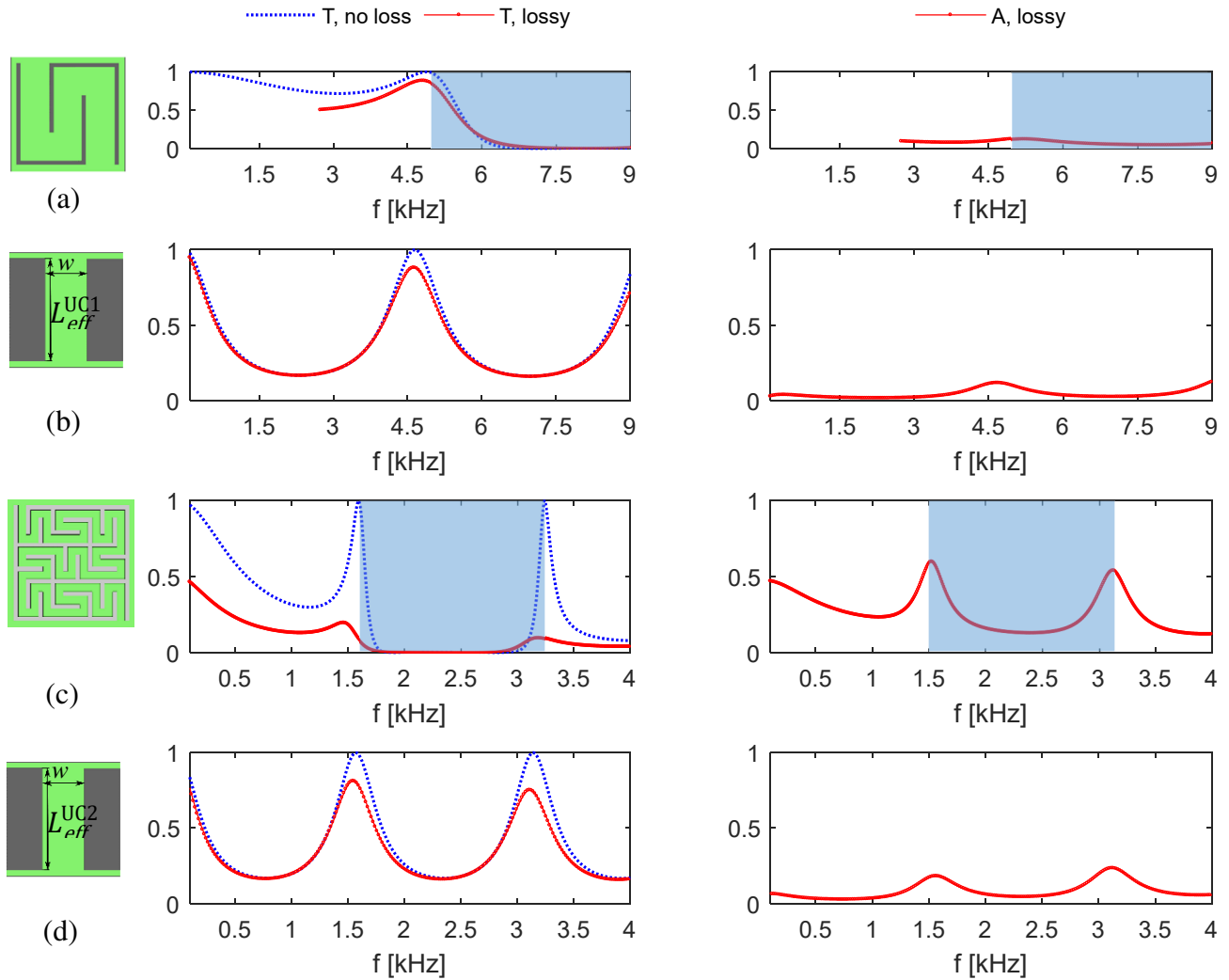
*Figure 8. **"Fixed unit cell" case:** Transmission (T) and absorption (A) coefficients for acoustic waves in lossless (dotted line) and lossy (solid line) air through (a) a labyrinthine unit cell UC1 and (b) a straight slit of width w = 3 mm and length L_{eff} = 34.6 mm; (c) a labyrinthine unit cell UC2 and (d) a straight slit of width w = 0.9 mm and length L_{eff} = 107 mm. Shaded regions indicate frequency band gaps.*